

On the use of the first-order moment approach for measurements of H_{eff} from LSD profiles

J.C. Ramírez Vélez¹*

¹*Instituto de Astronomía - Universidad Nacional Autónoma de México, APO. Postal 877, 22860, Ensenada B.C., Mexico*

Accepted XXX. Received TY; in original form ZZZ

ABSTRACT

The big majority of the reported measurements of the stellar magnetic fields that have analysed spectropolarimetric data have employed the least-square-deconvolution method (LSD) and the first-order moment approach. We present a series of numerical tests in which we review some important aspects of this technique. First, we show that the selection of the profile widths, i.e. integration range in the first-order moment equation, is independent of the accuracy of the magnetic measurements, meaning that for any arbitrary profile width it is always possible to properly determine the longitudinal magnetic field. We also study the interplay between the line depth limit adopted in the line mask and the normalisation values of the LSD profiles. We finally show that the rotation of the stars has to be considered to correctly infer the intensity of the magnetic field, something that has been neglected up to now. We show that the latter consideration is crucial, and our test shows that the magnetic intensities differ by a factor close to 3 for a moderate fast rotator star with $v \sin i$ of 50 km s^{-1} . Therefore, it is expected that in general the stellar magnetic fields reported for fast rotators are stronger than what was believed. All the previous results shows that the first-order moment can be a very robust tool for measurements of magnetic fields, provided that the weak magnetic field approximation is secured. We also show that when the magnetic field regime breaks down, the use of the first-order moment method becomes uncertain.

Key words: Stars : magnetic field – Technique: spectroscopic and polarimetric – Method : numerical.

1 INTRODUCTION

In the context of data analysis of circular polarisation in spectral lines, the development of the Centre-of-Gravity technique (CoG) was initially motivated to cater to a method for the measurement of the magnetic field of spatially resolved structures present in the solar photosphere (for example sunspots), without recourse to detailed theoretical modeling of circular polarisation in line profiles (Semel 1967). This approach establishes a linear relation between the component of the magnetic field vector projected along the line-of-sight (B_{LOS}) and the relative shift between the centres of gravity of the left and right components of the observed circular polarisation:

$$\lambda_+ - \lambda_- = 2\bar{g}\Delta\lambda_{B_{\text{LOS}}}, \quad (1)$$

where \bar{g} is the Lander factor of the transition line, $\Delta\lambda_{B_{\text{LOS}}}$ is the wavelength shift due to the Zeeman splitting, and

the centres of gravity for the left and right polarisation are respectively defined as (Rees & Semel 1979):

$$\lambda_{\pm} = \int_{-\infty}^{\infty} (I_c - (I \pm V)) \lambda d\lambda / \int_{-\infty}^{\infty} (I_c - (I \pm V)) d\lambda, \quad (2)$$

where I and V are the intensity and circular Stokes parameters, and I_c is the (assumed unpolarised) continuum. While from the previous definition the integration limits go from $-\infty$ to ∞ , in practice the integration spans only around the (full) width of the line profiles; therefore, the selection of the integration range –which can be subjective–, has an important impact in the accuracy of the magnetic field measurements. Since Eq. (2) corresponds to the first-order moment in λ , the CoG method is also known as the integral method for measurements of magnetic fields or simply as the first-order moment approach (e.g. Mathys 1989). Proven to be very useful, the CoG method was also applied in the stellar domain (e.g. Mathys 1991) to measure the mean longitudinal magnetic field –integrated over the visible hemisphere of the star–, also referred as the effective magnetic field (H_{eff}).

The CoG method was initially applied using the so-called photographic technique, however, with the develop-

* E-mail: jramirez@astro.unam.mx

ment of new instrumentation –CCDs and spectrographs of high resolution with better throughputs–, the helpful information contained in the shape of line profiles came at this disposal. Nowadays it is possible to simultaneously obtain a huge number of lines in spectropolarimetric mode with very high resolution.

The use of mean polarised profiles resulting from the addition of multiple individual lines in combination with the CoG method to infer H_{eff} , possible through the use of the LSD technique (Donati et al. 1997), was a benchmark in studies related to the stellar magnetism domain. By adding hundreds to thousands of individual lines, the signal-to-noise ratio of the mean circular polarised profile is increased by several orders of magnitude allowing the detection of extremely weak stellar magnetic fields with intensities in the order of few Gauss (e.g. Marsden et al. 2014). The use of the LSD lead to finding very interesting results in many types of stars and it also gave the opportunity to shape our current knowledge of the stellar magnetism by observational methods using multi-line spectropolarimetric data analysis (see e.g. Donati & Landstreet 2009).

For the addition of lines it is convenient to apply a variable transformation from wavelength to doppler velocity coordinates (v) (Semel 1995), such that the longitudinal stellar field would be given by (Mathys 1989; Donati et al. 1997):

$$H_{\text{eff}} = \frac{-7.145 \times 10^5}{\lambda_0 g_0} \frac{\int v \frac{V(v)}{I_c(v)} dv}{\int (1 - \frac{I(v)}{I_c(v)}) dv}, \quad (3)$$

where H_{eff} is expressed in G, v in km s^{-1} . If only weak and unblended lines are considered, λ_0 (expressed in nm) and g_0 would correspond respectively to the means of the wavelengths and Lander factors of the lines employed for the establishment of the mean profiles.

In fact, the CoG and the first-order moment approaches are valid under the following assumptions (Mathys 1989): 1) an atmospheric Milne-Eddington model, 1) a weak-line formation regime (that is when the line profile is similar in shape to the absorption coefficient (η), i.e. $\eta \ll 1$) and 3) are considered only weak magnetic fields (i.e. where the Zeeman splitting is much lower than the natural width of the line).

For the establishment of the mean profiles, if any of the 3 assumptions listed above is not fulfilled, or if blended lines are included, the value of $\lambda_0 g_0$ has to be found by independent calibration methods. This important statement will be in fact the subject of this paper, namely, we estimate H_{eff} through the first-order moment expressed in Eq. (3), and we inspect different criteria used during the establishment of the mean profiles. Example criteria include the line depth limit, the normalisation of the mean profiles and the integration limits. We also investigate the role played by projected rotational velocity of the stars ($v \sin i$) in the accuracy of the measurements of H_{eff} . Finally, all the results are discussed beyond the context of the weak field regime.

2 NUMERICAL TESTS

The employment of the linear relation given by Eq. (3) requires a proper calibration regulated solely by the product of the normalisation parameters g_0 and λ_0 . In this section

we will present a series of tests in which we obtained an optimal calibration through the use of theoretical spectra. We will denote these values by $\lambda_0 g_0$ to indicate that they were found by the methodology described below.

We have used the COSSAM code (Stift 2000) to synthesise a sample of 50 polarised spectra considering an oblique centred magnetic dipolar model (Stibbs 1950; Stift 1975). We have employed a solar atmospheric model: $T_{\text{eff}} = 5750$ K, $[M/H]=0$, $\log(g) = 4.5 \text{ cm s}^{-2}$, and microturbulence of zero, covering a wavelength range from 365 to 1010 nm in steps of 1 km s^{-1} . For our first test, we adopted a slow rotator model in which we assigned to $v \sin i$ a value of 5 km s^{-1} . For the synthesis of each spectrum, we have randomly varied the inclination between the 3 principal axis of the reference system, namely, the rotation axis, the magnetic dipolar axis and the line-of-sight direction. Considering only as free parameter these 3 angles that determine the orientation of the system, and setting the magnetic dipolar moment to 30 G, we obtained that in the synthetic sample the H_{eff} varies between -20 and 20 G.

For the establishment of the LSD profiles we have obtained from the VALD database (Ryabchikova et al. 2015) the information required to create the mask, i.e. for each line we retrieved from VALD the Lander factor, the line depth (d) and the wavelength. Using a line depth limit of 0.1 with respect the continuum as a threshold criteria, the total number of lines amounts to 8314. Of course, the same line list used in the mask was employed for the synthesis of the theoretical spectra in COSSAM. Since the synthetic sample of spectra is noiseless, we employed a cross-correlation between the mask and each spectrum to establish the sample of synthetic LSD profiles, and the mask weights that we assigned for the Stokes I and V parameters are those included in the original LSD-paper of Donati et al. (1997):

$$w_{Ii} = d_i; \quad w_{Vi} = d_i \lambda_i \bar{g}_i, \quad (4)$$

where the index i runs over the total number of lines.

The spectral resolution at which the theoretical spectra was synthesised (in wavelength steps of 1 km s^{-1}), has to be comparable to the instrumental one. Current observing facilities in spectropolarimetric mode have resolving powers (R) between 55,000 (CAOS) to 115,000 (HARPS). We thus decided to use the intermediate resolution of $R=65,000$ that corresponds to the twin spectrographs ESPADONS and NARVAL (and similar to the one in BOES, $R=60,000$). In consequence, we have decreased the resolution in the synthetic spectra to constant wavelength steps of 1.8 km s^{-1} to be consistent with the adopted resolution of these two spectrographs, reducing the total number of lines to 8088. Finally, to account for the instrumental broadening we convolved the spectra with a Gaussian kernel in which we considered a standard deviation in the Gaussian profile of 4.4 km s^{-1} .

In Fig. 1 we show some examples of the LSD profiles: one for the Stokes I (upper panel) and two for Stokes V in which the respective input magnetic models are such that the H_{eff} are -3.0 G (middle panel) and 8.5 G (lower panel). Even in this ideal case where no noise was added, by visual inspection it is not clear if the width of the two circular polarised profiles is the same. In other words, regarding the shown V profiles, we must consider whether to use the same width in both cases, and if yes, how to find it. Before tack-

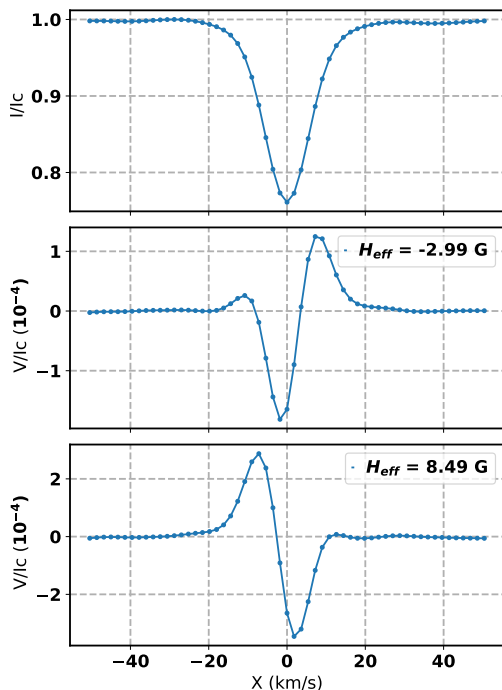


Figure 1. Examples of LSD profiles in intensity (upper panel) and circular polarisation (middle and lower panels). The longitudinal magnetical field for each V profile is indicated in an inner legend. The bin step in X –doppler coordinates– is of 1.8 km s^{-1} .

ling this issue in detail, let us note that many studies have employed a visual inspection to determine the width of the observed profiles (e.g. Wade et al. 2000; Silvester et al. 2009), and also that very early on Mathys (1988) was remarked the importance of a proper determination of the line width in an analysis under a n -order moment approach even in the case of one single line.

2.1 Profile width

We thus proceed to inspect how the considered integration limits in the doppler space –i.e. the LSD profiles width– can affect the inference of H_{eff} when using the first-order moment technique. For this purpose, we have varied the width of the profiles from 7.2 to 97.2 km s^{-1} around the line centre, in steps of 3.6 km s^{-1} . The adopted width variation at each step corresponds to considering one more point at each side of the line profile, i.e., the minimal possible difference when the profile width is varied symmetrically around the centre. For each considered profile width, we performed a linear regression over the 50 synthetic spectra to obtain the optimal value of $\lambda_0 \mathbf{g}_0$ that gives the best results to determine H_{eff} through Eq. (3). Note that it is not possible to obtain separately the values λ_0 and \mathbf{g}_0 , but only their product.

The results are shown in Fig. 2. In the upper panel we show the Mean Absolute Percental Error (MAPE) obtained by comparing the original values of H_{eff} and the ones derived

by the regressions¹, while the lower panel shows the respective fitted values of $\lambda_0 \mathbf{g}_0$, both as function of the integration limits (width profiles).

The first remark of this test is that for all considered profile widths, it is always possible to fit a value of $\lambda_0 \mathbf{g}_0$ that allows us to infer very accurately H_{eff} : the MAPE remains inferior to 1.0% in the big majority of the cases. This result is quite unexpected since even underestimating the width of the profiles up to the extreme case in which the profiles consist of only 5 central points (from -3.6 to 3.6 km s^{-1}), one can obtain very precise estimations of H_{eff} . Analogously, the same behaviour is obtained when the profiles are highly overestimated, with very small MAPE values. The fact that it is possible to consider deliberately only a part of the profiles to infer H_{eff} can be useful in some practical applications, as for example in binary systems or in stars surrounded by circumstellar envelopes with strong stellar winds that can generate shocks visible as bumps. The bump produced by the shock is in turn blended with the intensity profile of the star (e.g. Sabin et al. 2015), so to consider only a fraction of the intensity profile of the star could be of interest.

Another important result of this test is that it shows that the value of $\lambda_0 \mathbf{g}_0$ is very sensitive to the integration range, see lower panel of Fig. 2. The fitted values of $\lambda_0 \mathbf{g}_0$ start at 329 nm (profile width of 7.2 km s^{-1}) and they increase very quickly to reach a maximum of 918 nm (profile width of 21.6 km s^{-1}), to then decrease following a likely exponential-type curve, finishing at 286 nm for the broadest profile width of 97.2 km s^{-1} . Additionally, to illustrate the relative changes in the values of $\lambda_0 \mathbf{g}_0$, we take as reference a width of 39.6 km s^{-1} (from -19.8 to 19.8 km s^{-1}), which seems a plausible selection by visual inspection of the profiles in Fig. 1. In the right Y-axis of the lower panel in Fig. 2 are shown the percentage variations of $\lambda_0 \mathbf{g}_0$: as example, if one or two more points are considered at each side of the profiles, then the respective errors will overestimate the inferred H_{eff} by 7.5% and 16.0%. Similarly, an underestimation of H_{eff} of 6.5% and 12.5% will be induced if the width of the profiles is reduced by one and two points respectively.

Note that the polarised V profiles are almost zero around $\pm 20 \text{ km s}^{-1}$, and at first glance it could be surprising the fact that $\lambda_0 \mathbf{g}_0$ does not remain constant when the profile width continues to increase (integration range $> |20| \text{ km s}^{-1}$). The reason for this is due to the fact that the value of the integral in the denominator of Eq. (3) continues to vary even in the regions where the polarised signal is zero, and in consequence also $\lambda_0 \mathbf{g}_0$ varies to get an optimal fit.

One more interesting aspect to look at is if it is possible to consider asymmetric ranges of integration for the inference of H_{eff} . To answer this question, we have resized the sample of synthetic profiles from -19.8 to 7.2 km s^{-1} , and then we repeated the test. We found that in this case the errors are considerably higher: MAPE of 67%. Nevertheless, we verified that the inversion errors decrease as the asymmetry in the profiles decreases, reaching a value of 0.5% for the fully symmetric case (from -19.8 to 19.8 km s^{-1}). The conclusion is thus that the integration ranges have to be symmetric around the centre of profiles, but, as we showed above, the

$$^1 \text{MAPE}(\%) = \left| \frac{H_{\text{eff}}^{\text{original}} - H_{\text{eff}}^{\text{regression}}}{H_{\text{eff}}^{\text{original}}} \right|$$

Table 1. Self-consistency check of the measurements of H_{eff} and estimations of errors. The mean and standard deviations values are denoted by $\langle H_{\text{eff}} \rangle$ and σ , respectively. $H_{\text{eff}}^{\text{reg}}$ corresponds to the values obtained from the regression for different profile widths.

$\lambda_0 g_0$ (nm)	842.6	782.9	726.0	675.5	631.3	591.7	555.0	
Profile width (km s ⁻¹)	28.8	32.4	36.0	39.6	43.2	46.8	50.4	
	$H_{\text{eff}}^{\text{reg}}$	$H_{\text{eff}}^{\text{reg}}$	$H_{\text{eff}}^{\text{reg}}$	$H_{\text{eff}}^{\text{reg}}$	$H_{\text{eff}}^{\text{reg}}$	$H_{\text{eff}}^{\text{reg}}$	$H_{\text{eff}}^{\text{reg}}$	
$H_{\text{eff}}^{\text{original}} = 2.99$ G	-2.996	-2.993	-2.993	-2.995	-2.997	-3.000	3.005	$\langle H_{\text{eff}} \rangle \pm 3\sigma = 2.99 \pm 0.01$
$H_{\text{eff}}^{\text{original}} = 8.49$ G	8.492	8.496	8.497	8.495	8.491	8.486	8.479	$\langle H_{\text{eff}} \rangle \pm 3\sigma = 8.49 \pm 0.02$

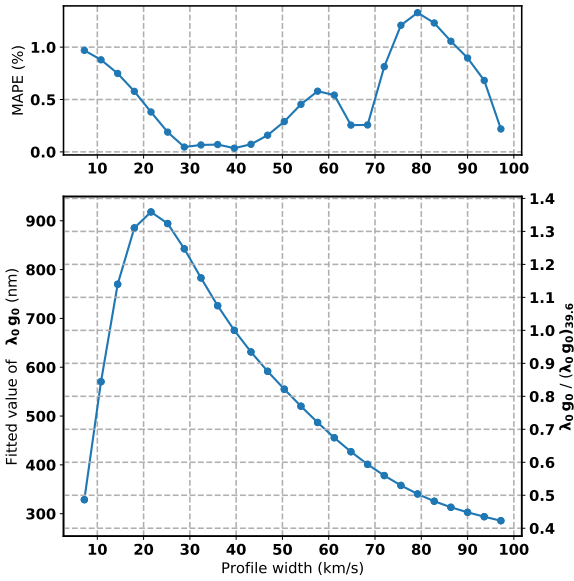


Figure 2. Mean absolute percentual error (upper panel) and normalisation values (lower panel) as function of the profiles width. In the right Y-axis of the lower panel, the values are normalised to the case when the profile width is 39.6 km s⁻¹. The results were obtained analysing a sample of 50 synthetic spectra.

integration ranges do not necessarily have to include the full width of the profiles.

The results of Fig. 2 allows to infer H_{eff} considering different profile widths, which in turn can be used for a check of the self-consistency of the measurements and to derive an associated uncertainty. Table 1, shows the obtained values of H_{eff} considering 7 different profile widths for the two LSD profiles shown in bottom of Fig. 1. The top of the central columns indicate the values of $\lambda_0 g_0$ and the respective profile widths.

The extremely high precision of H_{eff} reported in Table 1 are due to the fact that the sample of LSD profiles is noiseless. However, we consider that the mean and standard deviation values reflect a realistic value of the measurement of H_{eff} and the associated error, and could be especially useful for real observed data. Let us note that previous studies have shown that is very probable that the errors reported in studies based in LSD are underestimated (Carroll & Strassmeier 2014; Ramírez Vélez et al. 2018). In this sense, the *multi-inversions* strategy presented in Table 1, could be a good alternative to estimate the uncertainties.

Note that as it is customary, the calibration presented for the given values in T_{eff} and $\log(g)$, and for the given line list, can consider small variations; for example, in temperature a variation ± 125 K is still considered acceptable.

Given that the profiles used in this test are noiseless, we proceed to consider real data but not to continue the topic of this section, but to discuss another two important considerations as are the line depth limit adopted when establishing the LSD profiles, and the inclusion of noise-weighted masks.

2.2 Line depth and signals weighted by noise

When the analysis is applied to real data, the noise associated with the observations can be taken into account in different ways. In this section we will present some of them, which we consider the most employed ones.

Let us first introduce the so-called *mean weights* (MW) defined as (Marsden et al. 2014):

$$MW_1 = \frac{\sum_i S_i^2 w_{1i}^2}{\sum_i S_i^2 w_{1i}}; \quad MW_V = \frac{\sum_i S_i^2 w_{Vi}^2}{\sum_i S_i^2 w_{Vi}}, \quad (5)$$

where S_i is the inverse of the uncertainty derived from the data reduction process associated to the i th line (i.e. the signal-to-noise ratio of the i th line), and the weights w_{1i} and w_{Vi} are given by :

$$w_{1i} = \frac{d_i}{d_0^n}; \quad w_{Vi} = \frac{d_i \lambda_i \bar{g}_i}{d_0^n \lambda_0^n g_0^n}, \quad (6)$$

where the parameters d_0^n , λ_0^n and g_0^n are referred as the *normalisation values* (e.g. Kochukhov et al. 2010) or *scaling factors* (e.g. Petit et al. 2014). We have here adopted a different notation of the *normalisation values*, normally expressed also as λ_0 and g_0 . The reason of our notation is to avoid confusion because the *normalisation values* λ_0^n and g_0^n of Eq. (6) are not always the same as those used to derive H_{eff} in Eq. (3), i.e., $\lambda_0^n g_0^n \neq \lambda_0 g_0$.

Nowadays, when the line mask of the LSD profiles are established it is normally chosen that the *mean weights* are numerically equal or very close to unity. It is then assumed that the amplitude of the resulting LSD profiles is properly normalised by the definition adopted for the *mean weights*, and in consequence the normalisation parameters are directly used to measure H_{eff} in Eq. (3), i.e. $\lambda_0^n g_0^n = \lambda_0 g_0$.

As we mentioned, the *mean weights* are not the only way to normalise the LSD profiles. In fact, in the original LSD-paper of Donati et al. (1997), the authors proposed to scale the amplitudes of the profiles to $\lambda_0^n g_0^n d_0^n = 500$ nm and, to

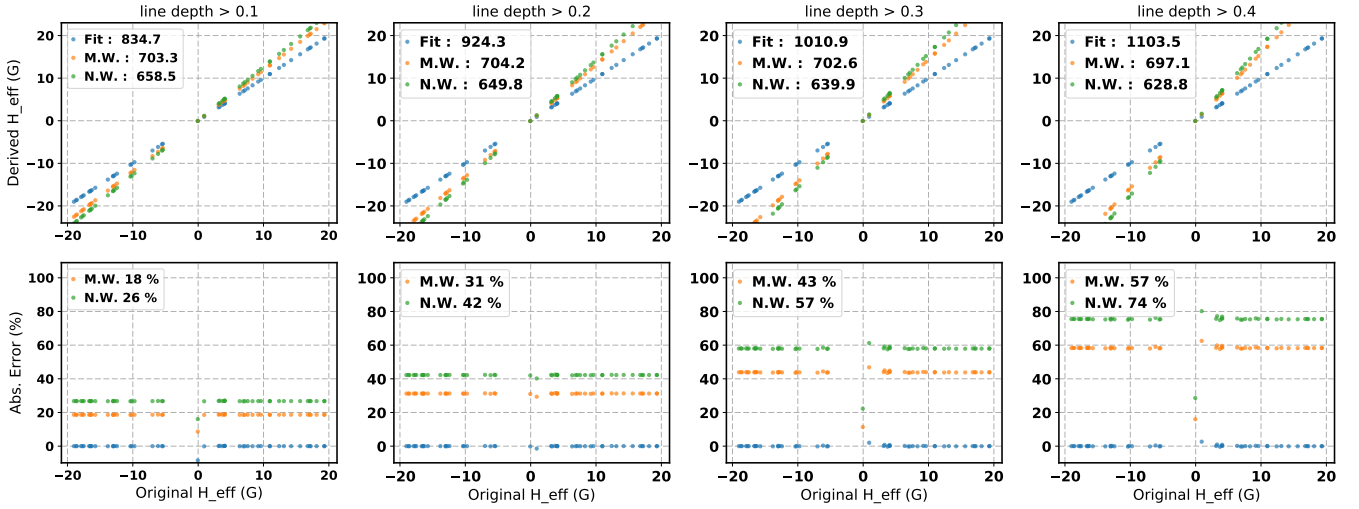


Figure 3. Upper panels: Computation between the original and derived vales of H_{eff} ; in blue the optimal fit ($\lambda_0 g_0$), in orange the *mean weights* ($\lambda_0^{\text{MW}} g_0^{\text{MW}}$) and in green the *noise weighted* ($\lambda_0^{\text{NW}} g_0^{\text{NW}}$) normalisation. Lower panels: Absolute percentual errors; the MAPE values for the *mean weights* and *noise weighted* approaches are included in the inner legends. The line depth threshold adopted is indicated on top of each column. The number of lines considered from left to right are 7757, 5688, 4517 and 3679, respectively.

use the mean values of λ_i and \bar{g}_i to measure H_{eff} in Eq. (3), i.e., $\lambda_0 = \langle \lambda_i \rangle$ and $g_0 = \langle \bar{g}_i \rangle$. This way of normalising the LSD profiles was used for some years, but the normalisation values changed by introducing a new constraint: $d_0^n = 0.7$ and at the same time $\lambda_0^n g_0^n d_0^n = 500$ nm (e.g. Wade et al. 2000; Shorlin et al. 2002; Donati et al. 2003, and others). It is important to mention that this approach to normalising the LSD profiles is not used anymore.

Alternatively, a *noise weighted* (NW) definition of the average values of λ_0 and g_0 has also been used in which the signal-to-noise ratio of the lines is included by the following expressions (e.g. Kochukhov et al. 2010; Grunhut et al. 2013):

$$\lambda_0 = \frac{\sum_i S_i^2 \lambda_i}{\sum_i S_i^2}; \quad \bar{g}_0 = \frac{\sum_i S_i^2 \bar{g}_i}{\sum_i S_i^2}. \quad (7)$$

In this *noise weighted* approach the average values are used to both, normalise the amplitude of the LSD profiles and to measure H_{eff} , i.e., $\lambda_0 = \lambda_0^n$ and $g_0 = g_0^n$.

We next compare two of the normalisation strategies presented above, namely, the *mean weighted* and the *noise weighted*. For the latter, the normalisation values, denoted by $\lambda_0^{\text{NW}} g_0^{\text{NW}}$, will be directly obtained through Eq. (7). For the former, given that MW_1 and MW_V are by construction equal to 1, the normalisation values, denoted by $\lambda_0^{\text{MW}} g_0^{\text{MW}}$, are given by:

$$d_0^{\text{MW}} = \frac{\sum_i S_i^2 d_i^2}{\sum_i S_i^2 d_i}; \quad \lambda_0^{\text{MW}} g_0^{\text{NW}} = \frac{\sum_i S_i^2 d_i^2 \lambda_i^2 \bar{g}_i^2}{d_0 \sum_i S_i^2 d_i \lambda_i \bar{g}_i}. \quad (8)$$

Additionally, we will include different values of the line depth limit, which is another important criteria when establishing the LSD profiles. In the published studies based in LSD, different line depth threshold values have been employed, from 5% to 40% with respect to the continuum, but the most commonly used ones are 10%, 20% and 40%. We

now proceed to quantify how much the value of the product of $\lambda_0 g_0$ varies when considering different line depth limits.

For this purpose, it is necessary to consider noise-affected data. Despite that it is always possible to model the noise following random or Poisson distributions, here we prefer to use real data. We have therefore obtained from *PolarBase* (Petit et al. 2014) the files associated with the solar twin type star HD63433, observed with the ESPaDOnS spectrograph at the CFHT telescope the 10 January 2010². In the files associated with the data reduction, we find the uncertainty in intensity that are the inverse of the S_i values required in Eqs. (7) and (8). We applied a linear interpolation to the wavelength sampling of the observed data to match the exact w_i values of the mask, which is a standard procedure. By considering the same spectral region in the synthetic sample and the observed data, the number of lines reduces to 7757 (with a line depth > 0.1). Besides, we have considered a value of $v \sin i = 7.0$ km s⁻¹ in the synthetic sample of spectra to be consistent with the value reported by Valenti & Fischer (2005) for the projected rotational velocity of HD63433.

Finally, in the previous section we have shown that $\lambda_0 g_0$ is dependent of the integration range in the doppler space (profile width). Therefore for this numerical test, we have fixed the profile width to 28.8 km s⁻¹, as indicated in the reduction log files of this observation. The integration limits that we considered vary from -14.4 to 14.4 km s⁻¹ in the rest frame of the star. The results are shown in Fig. 3.

The first remark of the results of this figure is that both, the *mean weights* and the *noise weighted* normalisation values, remain almost constant. By changing the threshold of the line depth from 0.1 to 0.4, the values of $\lambda_0^{\text{MW}} g_0^{\text{MW}}$ shows a decrease of only $\sim 1\%$ (from 703 to 697 nm), while for

² The block reference number of this observation in the *PolarBase* database is 8450.

$\lambda_0^{\text{MW}} g_0^{\text{MW}}$ the decrement is $\sim 5\%$ (from 659 to 629 nm). On the contrary, the optimal fit obtained for $\lambda_0 g_0$ increases in 32% (from 835 to 1104 nm). In consequence, it is shown from left to right in the lower panels of Fig. 3, that the errors increase from 18% to 56% for the *mean weight* estimations of H_{eff} , while for the *noise weight* approach the errors are even higher passing from 26% to 74%.

The conclusion of this test is that for each observation, or equivalently for each set of given values of S_i , there is only one value of line depth that fulfils $\lambda_0 g_0 = \lambda_0^{\text{MW}} g_0^{\text{MW}}$, and analogously only one other such that $\lambda_0 g_0 = \lambda_0^{\text{NW}} g_0^{\text{NW}}$. For the case presented here, those two values are inferior to a line depth limit of 0.1. Therefore, it is not convenient to search for which line depth value the *mean weights* or *noise weighted* are good normalisations, but the contrary, that given any limit for the line depth, the values of $\lambda_0 g_0$ must be found through synthetic spectra, as we have proceeded here. Currently, some studies indicate that $\lambda_0 g_0$ are derived through synthetic spectra, however the procedure is not described and the values of $\lambda_0 g_0$ are in general only announced.

2.3 V_{sini}

In this section, we will focus on inspecting whether the estimations of the stellar longitudinal magnetic field can be affected by the rotation of the star, an effect normally ignored, and if yes how important it is to consider the v_{sini} value in the synthetic sample of spectra. In fact, by increasing the projected rotational speed of the star, two important effects appear. First, the blending of the lines increases, and second, the weak-line regime is less justified up to the case in which the shape of the line profile is rotationally dominated. With the aim of investigating the resultant interplay of these two effects, we present an estimation of the $\lambda_0 g_0$ values as function of v_{sini} .

We have considered the same solar atmospheric model as in the previous tests, with the only difference that now the projected rotational values are varied from 0 to 50 km s^{-1} in steps of 5 km s^{-1} . For each of these v_{sini} values, we synthesised a sample of 50 spectra to then fit a linear regression obtaining in each case $\lambda_0 g_0$.

Before continuing, it is essential to define the integration limits for each of the v_{sini} values. We have visually inspected simultaneously both Stokes profiles, I and V, to define their widths. Strategies other than visual inspection could be adopted but for the main purpose of this test (to determine the variation of $\lambda_0 g_0$ as function of v_{sini}), we consider that the employed strategy is enough. Fig. 4 shows in colour the selected profile widths, and in black the remaining part of the profiles for all the rotational values.

For comparison purposes, in the establishment of the LSD profiles we have considered two different values of the line depth limit, 0.1 and 0.4. The results shown in Fig. 5 are presented as before: the upper panel shows the precision of the inversions quantified through the MAPE values and the lower one shows the fitted values $\lambda_0 g_0$, both as function of v_{sini} . For completeness, below the curve of line depth limit of 0.1 of the lower panel, we have included the profile width employed at each rotational value: For example, for a v_{sini} of 10 km s^{-1} , the indicated profile width is 43.2 km s^{-1} , which

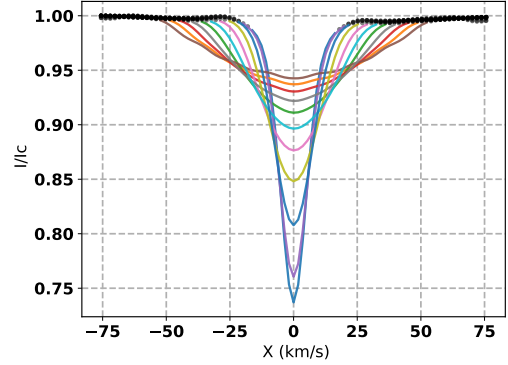


Figure 4. In colour the profile widths that determine the integration limits to infer H_{eff} . The profiles correspond to different values of v_{sini} that vary from 0 to 50 km s^{-1} in constant steps of 5 km s^{-1} .

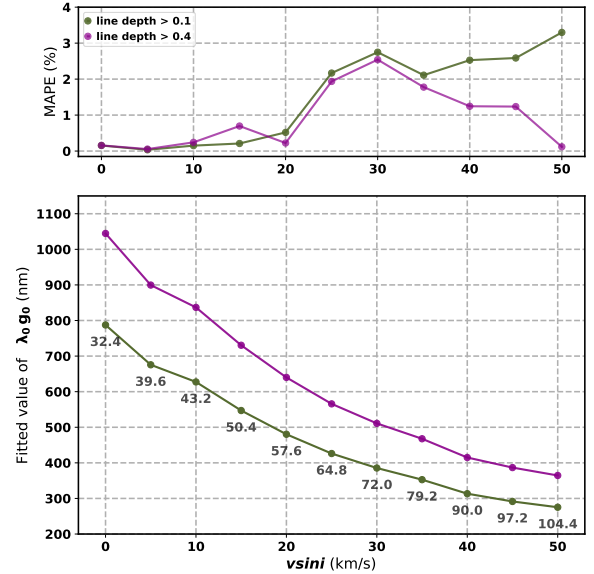


Figure 5. Mean absolute percentual error (upper panel) and normalisation values (lower panel) as function of v_{sini} , considering line depth limits of 0.1 (in green) and 0.4 (in magenta). The numbers below the green line in the lower panel indicate the considered width of the profiles.

means that the integration range goes from -21.6 to 21.6 km s^{-1} in the rest frame of the star.

The results from Fig. 5 indicate that for all the rotational values the retrieved values of H_{eff} are very good: except in one case the MAPE is always less than 3%. Therefore, with this test it is shown that even in the case with the strongest rotation velocity of 50 km s^{-1} , whose shape profile is clearly dominated by the rotation and the blending process are the highest, the first-order moment is still a very good tool to measure the longitudinal magnetic field. However, good precision of estimations of H_{eff} requires an appropriate value $\lambda_0 g_0$ for each rotational value. In fact, the normalisation value changes by a factor close to 3 when passing from extreme to the other of the v_{sini} values, from

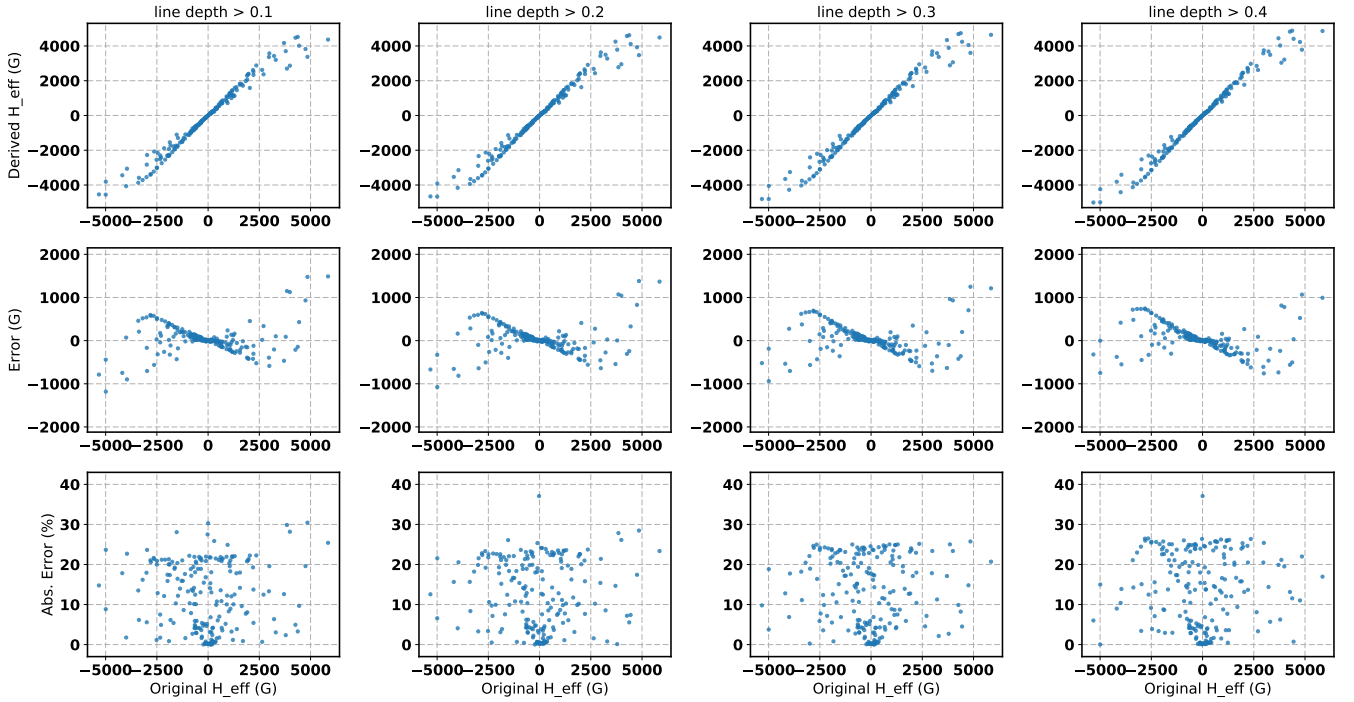


Figure 6. Comparison of the input and inferred H_{eff} values (upper panels). The errors are shown in units of Gauss (middle panels) and in absolute percentage (lower panels).

0 to 50 km s^{-1} . In other words, if the $\lambda_0 \mathbf{g}_0$ corresponding to a null rotational value is employed to infer H_{eff} for a moderate fast rotator star with a $v \sin i$ of 50 km s^{-1} , our results indicate the magnetic fields will be underestimated by 287% (the same percentage was found for both line depth limits of 0.1 and 0.4). The conclusion of this test is therefore that it is mandatory to consider the projected rotational velocity of the stars when determining the normalisation values $\lambda_0 \mathbf{g}_0$, something that has been neglected up to today.

Please note that similar results have been obtained not on the basis of the integral form (Eq. 3) but rather on the derivate one. Recently, using the slope method, [Scalia et al. \(2017\)](#) have also shown that the errors of the longitudinal magnetic field increase when the $v \sin i$ increases, while [Leone et al. \(2017\)](#) indicate that H_{eff} is properly estimated only for rotational velocities lower than 12 km s^{-1} .

2.4 Magnetic field intensities

In the previous sections we have purposely performed the tests in a regime where the weak magnetic field assumption was assured : $|H_{\text{eff}}| < 20 \text{ G}$, and the magnetic moment was fixed to 30 G . We are now interested in considering stronger intensities in the magnetic fields.

For the next numerical exercise, we synthesised a sample of 200 stellar spectra with the same atmospheric model as before, adopting a $v \sin i$ value of 5 km s^{-1} , but now the magnetic moment was increased up to two more orders of magnitude, varying between 0.1 and 10 kG . The reason that we have considered a higher number of synthetic spectra is to better sample H_{eff} , which varies in a wider range of intensities, between -6 and 6 kG .

For the inference of H_{eff} , in Eq. (3) we have used the value $\lambda_0 \mathbf{g}_0 = 675.5 \text{ nm}$ that was found previously when only weak magnetic fields were considered, the line depth limit was 0.1, $v \sin i = 5 \text{ km s}^{-1}$, and the integration limits varied between -19.6 to 19.6 km s^{-1} , see Table 1. The sample of spectra for this test was in consequence inverted using this same range of the integration. For completeness, we have also considered the line depth threshold values of 0.2, 0.3 and 0.4. For each of these cases, we have considered the values of $\lambda_0 \mathbf{g}_0$ derived previously under a weak magnetic field regime, which are 749.0 , 822.6 and 899.6 nm , respectively. The results are shown in Fig. 6. Before to discuss the results, it is important to note that these do not depend on the integration range. We have verified that by changing the profiles width (integration range), the results are in essence the same.

The first remark of this test is that the results are the same despite the line depth cut-off value considered in the mask (indicated in top each column). The second is that it is not possible (in function of H_{eff}) to constrain where the weak magnetic field regime breaks down, given that for both the weakest ($< 500 \text{ G}$) and the strongest ($> 2 \text{ kG}$) intensities, it is possible achieve very accurate values of H_{eff} in some cases, but the errors can reach 25% to 30% in others. Thus, the conclusion of this test is that with a dipolar magnetic configuration, and considering random orientations of the principal axis of the system, it is unfortunately not possible to a priori set a limit to the validity of the weak field approximation using as constrain H_{eff} .

A clear interpretation of the results of Fig. 6 can be obtained in terms of the surface magnetic field (H_{surf}), defined as the mean of the local magnetic field moduli. In Fig. 7, we

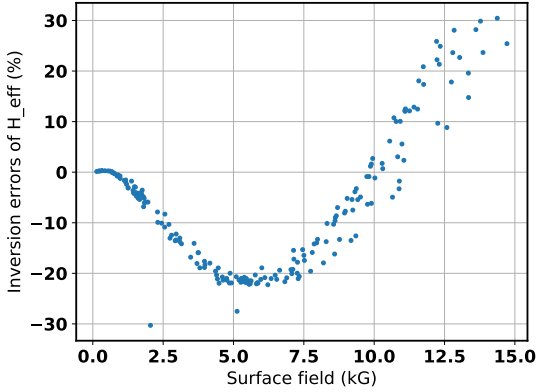


Figure 7. Percentual errors of H_{eff} , given by $\frac{H_{\text{eff}}^{\text{ori}} - H_{\text{eff}}^{\text{reg}}}{H_{\text{eff}}^{\text{ori}}}$, as function of magnetic surface field. The results correspond to a line depth limit of 0.1.

show the inversion errors of H_{eff} as function of H_{surf} . In this case, it is evident that when the weak magnetic field regime is assured the inversions errors are extremely low. However, around 1 kG the weak magnetic field assumption starts to not be valid and in consequence the inversion errors –which overestimate H_{eff} – begin to increase, reaching a maximum of 20% for surface fields around 5 kG. Surprisingly, when the surface intensities continue to increase, the overestimation of H_{eff} starts to decrease, is close to zero around 10 kG and then inversion errors begin to underestimate H_{eff} . There is no clear explanation for this empirical behaviour, and more tests should be carried out to inspect it in detail, something that is beyond the scope of this study.

Unfortunately once more, the fact that inversions error of the magnetic longitudinal field can be constrained by the surface field intensity, it is not useful in practice for the analysis of snapshot spectropolarimetric observations, since for this it is required to know the distribution of the local magnetic fields over the star. However, the results of Fig. 6 are helpful for the magnetic imaging technique.

In order to disentangle the limitations of LSD profiles separately of those of the the first-order moment approach, we will now employ other technique to derive H_{eff} , namely, machine learning algorithms. In [Ramírez Vélez et al. \(2018\)](#), we have shown that these algorithms are indeed very accurate for measurements of longitudinal magnetic fields, with MAPE values similar to the ones found in previous sections.

Using the same sample of 200 synthetic spectra of Figs. 6 and 7, we have trained an Artificial Neuronal Network (ANN). The proper functioning of the ANN was performed using a K-fold = 5 validation test, which means that the full sample of 200 spectra is divided in five subsamples. Then, each subsample (consisting of 40 spectra) is used to train the ANN, and the inversions are performed over the remaining 160 spectra. This, process is repeated for all subsamples, and the obtained validation coefficient was 0.99 ([Ramírez Vélez et al. 2018](#), in particular, all the technical details about the ANN are given in the appendix of that work). The results obtained with the ANN trained with the LSD profiles are shown in Fig. 8.

It is clear from the right columns of Fig. 8 that to use a

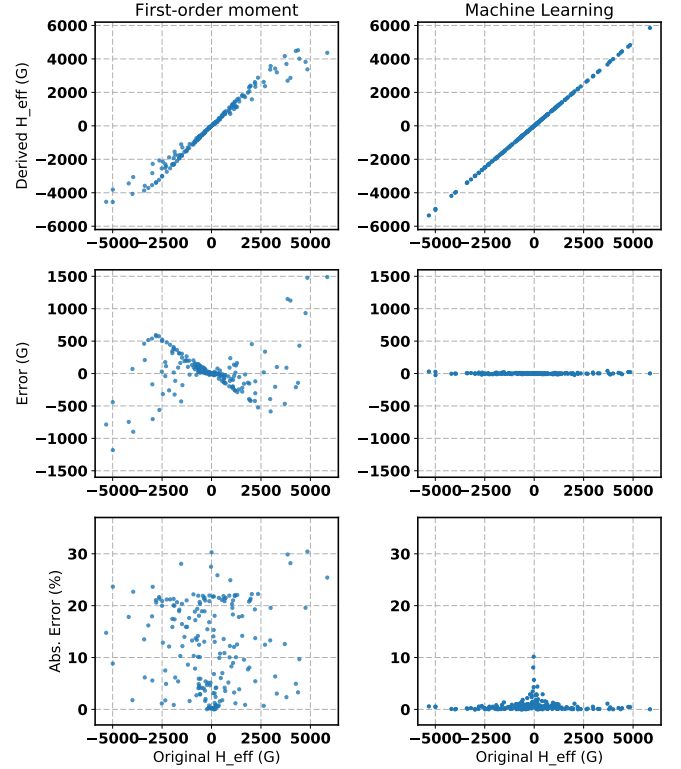


Figure 8. Comparison of the inversions results of both techniques, the first-order moment approach (left columns) and the Artificial Neuronal Network (right columns). The sample of synthetic profiles is the same in both columns, and corresponds to the case of a line depth limit of 0.1.

sample of LSD profiles to train a machine learning algorithm allows to determine H_{eff} very precisely for all magnetic intensities, from -6 to 6 kG. In consequence, it is demonstrated with this test that the inaccuracy of the results of Figs. 6 and 7 is due to the use of the first-order moment approach and not to the LSD profiles.

3 CONCLUSIONS

The present study is not the first one to highlight the crucial role played by normalisation parameters when measuring the magnetic stellar field through the LSD profiles. [Kochukhov et al. \(2010\)](#) have already stated that the same values to normalise the LSD profiles must be the same ones used in the first-order moment formula, i.e. $\lambda_0 g_0 = \lambda_0^n g_0^n$. That is in fact what we found in the controlled tests of the previous section. We stress that it is always possible to use any of the mean strategies – either the simple mean $\langle \lambda_i \rangle < \bar{g}_i \rangle$, the *mean weighted* or the *mean noise weighted*–, but for these approaches it is required to a priori find the value of line depth for which the mean values will be equal to $\lambda_0 g_0$.

Regardless of the employed normalisation strategy and considering that $\lambda_0 g_0$ are found through synthetic spectra, there are still two important considerations normally set aside. The first one, already discussed, is that the normalisation values are dependent on *vsini*. One of the reasons that

the dependence in $v \sin i$ was ignored is due to the fact that it was assumed that all lines are autosimilars, something that is clearly not the case for different rotational values with different line blendings. The second one is that many recent publications have analysed samples of stars in which the mask of each star is carefully established but the normalisation values are the same for all the stars, despite that in the sample the stars have different atmospheric parameters as T_{eff} , $\log(g)$, $v \sin i$, etc. (e.g. Alecian et al. 2013; Villebrun et al. 2019; Hill et al. 2019).

Our results concerning the integration range of Eq. (3), is contrary to what other previous studies announced where it was stated that there is only one *appropriate* width of the LSD profiles that allows to correctly determine H_{eff} (e.g. Neiner et al. 2012). Here, we have shown that even taking a small portion of the full width of the profiles, or to highly overestimate the width of the profiles, is useful to correctly determine H_{eff} (if $\lambda_0 g_0$ is previously found for each profile width and if the integration limits are symmetrical around the centre of profiles). Moreover, given that it is possible to use different profile widths, i.e. different integration limits in Eq. (3), we proposed a method to estimate the incertitude of the measurements using the *multi-inversions* strategy (see Table 1).

In fact, the main conclusion of this work is that the use of the first-order moment technique for the measurement of H_{eff} from multi-line LSD profiles is a very robust approach if and only if the parameters $\lambda_0 g_0$ of Eq. (3) are properly determined and provided that the weak magnetic field regime is fulfilled. We showed that a sound methodology to find $\lambda_0 g_0$ is through the use of a small sample of theoretical spectra calculated with the physical parameters as close as possible to the data one wish to analyse. In this respect, please note that we have inspected only those physical parameters that we consider to be the ones which have more impact in the first-order approach, but we have left out many other parameters such as micro and macro turbulence, metallicity, $\log(g)$, and others, which we considered to have a less impact on the linear relation given by Eq. (3).

There is no doubt that with the results shown in this work some of the previous reported measurements of stellar magnetic fields, through a combined analysis of LSD profiles and the first-order moment method, deserve to be revised. More importantly, new studies using the first-order moment technique must properly calibrate $\lambda_0 g_0$ in order to give more accuracy to the results. This fact is likely crucial for fast rotator stars, in which it seems that the magnetic fields reported for these stars have been systematically underestimated. With case study presented here where a solar atmospheric model was considered, the underestimation reached almost 300% around $v \sin i \sim 50 \text{ km s}^{-1}$. The final conclusion is that in general the intensities of magnetic fields in fast rotators stars, where H_{eff} has been measured through the first-order moment and the LSD profiles, is expected to be more intense than believed.

Finally, we also showed that very good measurements of H_{eff} are no longer possible if the magnetic weak field assumption is not valid. With the magnetic dipolar model employed to establish the polarised synthetic samples, we could not find a critical value of H_{eff} from which the weak field approximation breaks down. In other words, extremely weak measured values of H_{eff} do not assure the weak field regime.

This fact is a consequence of the well known effect of attenuation of circular polarised signals due to the balance of positive and negative polarities of the magnetic field over the visible hemisphere of the star.

We also showed how to overcome this problem by using alternative methods as are the machine learning algorithms (Ramírez Vélez et al. 2018). Using the same sample of LSD profiles, we could properly infer the values of H_{eff} for the full sample of LSD profiles, including strong intensities in the order of kG (Fig. 8). This demonstrates that the main constrain when deriving the stellar longitudinal magnetic fields are not the LSD profiles, but the use of the first-order moment approach, which is based in assumptions that can be very restrictives in practice given that the value of H_{eff} does not allow a priori determine if the weak field approximation is assured.

ACKNOWLEDGEMENTS

The author thanks to Franco Leone for helpful discussions that helped to improve the content of the manuscript. This study has been supported by UNAM through the PAPIIT grant number IN103320.

REFERENCES

- Alecian E., et al., 2013, *MNRAS*, **429**, 1001
 Carroll T. A., Strassmeier K. G., 2014, *A&A*, **563**, A56
 Donati J.-F., Landstreet J. D., 2009, *ARA&A*, **47**, 333
 Donati J.-F., Semel M., Carter B. D., Rees D. E., Collier Cameron A., 1997, *MNRAS*, **291**, 658
 Donati J. F., et al., 2003, *MNRAS*, **345**, 1145
 Grunhut J. H., et al., 2013, *MNRAS*, **428**, 1686
 Hill C. A., Folsom C. P., Donati J. F., Herczeg G. J., Hussain G. A. J., Alencar S. H. P., Gregory S. G., Matysse Collaboration 2019, *MNRAS*, **484**, 5810
 Kochukhov O., Makaganiuk V., Piskunov N., 2010, *A&A*, **524**, A5
 Leone F., Scalia C., Gangi M., Giarrusso M., Munari M., Scuderi S., Trigilio C., Stift M. J., 2017, *ApJ*, **848**, 107
 Marsden S. C., et al., 2014, *MNRAS*, **444**, 3517
 Mathys G., 1988, *A&A*, **189**, 179
 Mathys G., 1989, *Fundamentals Cosmic Phys.*, **13**, 143
 Mathys G., 1991, *A&AS*, **89**, 121
 Neiner C., Alecian E., Briquet M., Floquet M., Frémat Y., Martayan C., Thizy O., Mimes Collaboration 2012, *A&A*, **537**, A148
 Petit P., Louge T., Théado S., Paletou F., Manset N., Morin J., Marsden S. C., Jeffers S. V., 2014, *PASP*, **126**, 469
 Ramírez Vélez J. C., Yáñez Márquez C., Córdoba Barbosa J. P., 2018, *A&A*, **619**, A22
 Rees D. E., Semel M. D., 1979, *A&A*, **74**, 1
 Ryabchikova T., Piskunov N., Kurucz R. L., Stempels H. C., Heiter U., Pakhomov Y., Barklem P. S., 2015, *Phys. Scr.*, **90**, 054005
 Sabin L., Wade G. A., Lèbre A., 2015, *MNRAS*, **446**, 1988
 Scalia C., Leone F., Gangi M., Giarrusso M., Stift M. J., 2017, *MNRAS*, **472**, 3554
 Semel M., 1967, *Annales d'Astrophysique*, **30**, 513
 Semel M., 1995, in Comte G., Marcellin M., eds, *Astronomical Society of the Pacific Conference Series Vol. 71*, IAU Colloq. 149: Tridimensional Optical Spectroscopic Methods in Astrophysics. p. 340

- Shorlin S. L. S., Wade G. A., Donati J. F., Land street J. D.,
Petit P., Sigut T. A. A., Strasser S., 2002, *A&A*, **392**, 637
- Silvester J., et al., 2009, *MNRAS*, **398**, 1505
- Stibbs D. W. N., 1950, *MNRAS*, **110**, 395
- Stift M. J., 1975, *MNRAS*, **172**, 133
- Stift M. J., 2000, *A Peculiar Newsletter*, **33**, 27
- Valenti J. A., Fischer D. A., 2005, *ApJS*, **159**, 141
- Villebrun F., et al., 2019, *A&A*, **622**, A72
- Wade G. A., Donati J. F., Landstreet J. D., Shorlin S. L. S., 2000,
MNRAS, **313**, 851